

On the modeling of wave–current interaction using the elliptic mild-slope wave equation

Wei Chen^a, Vijay Panchang^{b,*}, Zeki Demirebilek^c

^a*Pacific International Engineering, PLLC, Edmonds, WA 98020, USA*

^b*Department of Maritime Systems Engineering, Texas A&M University, Galveston, TX 77553, USA*

^c*Coastal Hydraulics Laboratory, Army Engineering R&D Center, Vicksburg, MS 39180, USA*

Received 15 November 2004; accepted 28 February 2005

Available online 16 June 2005

Abstract

Methods to incorporate the effect of ambient currents in the prediction of nearshore wave transformation are developed. This is accomplished through the construction of a finite-element coastal/harbor wave model based on an extended mild-slope wave–current equation that includes wave breaking. Improved boundary conditions are used to provide more accurate forcing and to minimize spurious wave reflections from the boundaries. Multiple nonlinear mechanisms, appearing both in the governing equations and in the boundary conditions, are handled successfully and efficiently with iterative techniques. The methods are tested against results from other types of models based on parabolic approximations or Boussinesq equations for three wave–current problems of common interest and varying complexity. While indicating good agreement in general, the analysis also highlights the limitations of parabolic approximation models in case of strong local currents and velocity shear. We also consider the harbor engineering problem pertaining to waves approaching an inlet with a jettied entrance, where wave–current interaction can create a complex wave pattern that adversely affects small craft navigation and causes scouring. The role of ebb and flood currents on wave transformation and on breaking in the vicinity of the inlet is investigated using the model in conjunction with hydraulic laboratory data. It is found that although the ebb currents cause larger waves outside the inlet, much of the wave energy is soon dissipated due to breaking; during the flood tide, in contrast, more wave energy can penetrate into the inlet throat. © 2005 Elsevier Ltd. All rights reserved.

Keywords: Mild-slope equation; Elliptic wave model; Wave–current interaction

* Corresponding author.

E-mail addresses: weic@piengr.com (W. Chen), panchanv@tamug.tamu.edu (V. Panchang), zeki.demirebilek@erdc.usare.army.mil (Z. Demirebilek).

Report Documentation Page				Form Approved OMB No. 0704-0188	
Public reporting burden for the collection of information is estimated to average 1 hour per response, including the time for reviewing instructions, searching existing data sources, gathering and maintaining the data needed, and completing and reviewing the collection of information. Send comments regarding this burden estimate or any other aspect of this collection of information, including suggestions for reducing this burden, to Washington Headquarters Services, Directorate for Information Operations and Reports, 1215 Jefferson Davis Highway, Suite 1204, Arlington VA 22202-4302. Respondents should be aware that notwithstanding any other provision of law, no person shall be subject to a penalty for failing to comply with a collection of information if it does not display a currently valid OMB control number.					
1. REPORT DATE 16 JUN 2005		2. REPORT TYPE N/A		3. DATES COVERED	
4. TITLE AND SUBTITLE On the Modeling of Wave-Current Interaction Using the Elliptic Mild-Slope Wave Equation				5a. CONTRACT NUMBER	
				5b. GRANT NUMBER	
				5c. PROGRAM ELEMENT NUMBER	
6. AUTHOR(S) ; ; Chen /WeiPanchang /Vijayand Demirbilek /Zemi				5d. PROJECT NUMBER	
				5e. TASK NUMBER	
				5f. WORK UNIT NUMBER	
7. PERFORMING ORGANIZATION NAME(S) AND ADDRESS(ES) Pacific International Engineering, PLLC, Edmonds, WA; Department of Maritime Systems Engineering, Texas A&M University, Galveston, TX; Army Engineer Research and Development Center, Coastal and Hydraulics Laboratory, Vicksburg, MS				8. PERFORMING ORGANIZATION REPORT NUMBER	
9. SPONSORING/MONITORING AGENCY NAME(S) AND ADDRESS(ES)				10. SPONSOR/MONITOR'S ACRONYM(S)	
				11. SPONSOR/MONITOR'S REPORT NUMBER(S)	
12. DISTRIBUTION/AVAILABILITY STATEMENT Approved for public release, distribution unlimited.					
13. SUPPLEMENTARY NOTES					
14. ABSTRACT This document develops methods to incorporate the effect of ambient currents in the prediction of nearshore wave transformation through the construction of a finite-element coastal/harbor wave model based on an extended mild-slope wave-current equation that includes wave breaking. The methods are tested against results from other types of models based on parabolic approximations or Boussinesq equations for three wave-current problems of common interest and varying complexity. While indicating good agreement in general, the analysis also highlights the limitations of parabolic approximation models in case of strong local currents and velocity shear. Also considered is the harbor engineering problem pertaining to waves approaching an inlet with a jettied entrance, where wave- current interaction can create a complex wave pattern that adversely affects small craft navigation and causes scouring. The role of ebb and flood currents on wave transformation and on breaking in the vicinity of the inlet is investigated using the model in conjunction with hydraulic laboratory data. It is found that although the ebb currents cause larger waves outside the inlet, much of the wave energy is soon dissipated due to breaking; during the flood tide, in contrast, more wave energy can penetrate into the inlet throat.					
15. SUBJECT TERMS					
16. SECURITY CLASSIFICATION OF:			17. LIMITATION OF ABSTRACT UU	18. NUMBER OF PAGES 30	19a. NAME OF RESPONSIBLE PERSON
a. REPORT unclassified	b. ABSTRACT unclassified	c. THIS PAGE unclassified			

1. Introduction

Reliable prediction of wave motion in coastal areas is crucial to coastal engineering applications associated with nearshore morphologic change and harbor/inlet maintenance. Wave transformation in shallow coastal areas occurs largely as a consequence of bathymetric variations and domain geometry, and several modeling methods that can reliably predict the resulting refraction, diffraction, reflection, and dissipation are now used in practice (e.g. Vogel et al., 1988; Kirby and Dalrymple, 1994; Panchang and Demirebilek, 2001). In some areas, however, ambient tidal and other currents can be strong and their effect on wave transformation can be substantial. They create a Doppler shift and cause wave refraction, reflection, and breaking, which can result in overall redistribution of wave energy.

In this paper, we develop techniques for simulating the effects of ambient currents on wave transformation in coastal areas with arbitrary geometry using the finite element method. Our focus is on phase-resolving models that are based on a mass-balance formulation, as opposed to the energy-balance (phase averaged) models such as SWAN (Booij et al., 1999; Ris et al., 1999) and STWAVE (Resio, 1993). While energy-balance wave models are suited to large scale wave growth and wave transformation applications, phase-resolving wave models are better suited to domains with complex bathymetric and geometric features, where the effects of wave diffraction and reflection can be important. Phase resolving models are based on the elliptic mild or steep-slope equation (e.g. Berkhoff, 1972; Chamberlain and Porter, 1995), which is applicable to the full spectrum of water waves, or on the Boussinesq equations (e.g. Madsen and Sørensen, 1992; Nwogu, 1993; Wei et al., 1995), which are traditionally limited to shallow water waves. Each of these approaches is accompanied by its own set of modeling difficulties, as described in the review by Panchang et al. (1998). Here, we limit our approach to the former type of models, which is based on the extension of Berkhoff's mild-slope equation (Kirby, 1984) that includes the effect of ambient currents.

Solving the elliptic equation presents considerable computational difficulties, as detailed by Panchang et al. (1991) and Grassa and Flores (2001) involving wave–current interaction further complicates the problem. Existing models based on the extended wave–current equation have, therefore, relied on various approximations. For example, Liu (1983) and Kirby and Dalrymple (1994) have used the ‘parabolic approximation’ in which a solution can easily be obtained by marching forward from one computational row to the next. However, this method places restrictions on the direction of wave propagation and is hence applicable to cases with limited refraction and diffraction and with no reflection. Li and Anastasiou (1992) proposed solving the extended elliptic governing equation using a combination of the multigrid finite difference method and a logarithmic transformation of the velocity potential. The transformation, as noted by Radder (1992), yields inaccurate predictions near complex bathymetries; and the multigrid method, like the parabolic approximation, is best suited to modeling domains of simple shape such as rectangular domains. Further, if the current pattern is complex, the effects of these limitations are likely to be exacerbated.

Here, we present a comprehensive treatment of several issues associated with finite-element modeling of wave–current interaction using the mild-slope equation.

(The treatment is identical for the steep-slope equation of Chamberlain and Porter, 1995). We tackle the full elliptic version of the extended wave–current equation with improved treatment of boundary conditions, intending to better accommodate two-dimensional wave scattering phenomena in domains with arbitrary geometry and complex current fields. Wave breaking due to currents and bathymetry is also included, using the formulation of Battjes and Janssen (1978).

The work described here is an extension of recent developments in finite-element elliptic wave modeling (Kostense et al., 1988; Xu et al., 1996; Panchang et al., 2000; Zhao et al., 2001; Chen et al., 2002, etc.). The layout of this paper is as follows. After presenting the governing equations in Section 2, we develop appropriate boundary conditions for two kinds of problems in Section 3. Section 4 describes the solution method and numerical techniques for handling multiple nonlinear mechanisms. In Section 5, three test cases for model validation are described. In Section 6, numerical results are used in conjunction with hydraulic model data to investigate the harbor engineering problem involving waves approaching a harbor through a jettied inlet in the presence of ebb and flood currents. Concluding remarks are given in Section 7.

2. Governing equations

Kirby (1984) modified the earlier works of Booij (1981) and Liu (1983) and derived the following extension of the mild-slope equation that includes the effect of background currents:

$$\frac{D^2 \Phi}{Dt^2} + (\nabla \cdot \vec{U}) \frac{D\Phi}{Dt} - \nabla \cdot (CC_g \nabla \Phi) - (k^2 CC_g - \sigma^2) \Phi = 0 \quad (1)$$

where the operator $D/Dt = (\partial/\partial t + \vec{U} \cdot \nabla)$, $\vec{U}(x, y) = (u, v)$ is the current field, and $\Phi(x, y, t)$ is the complex velocity potential at mean water surface. The wave number k and the intrinsic wave frequency σ may be determined through the linear dispersion relation and the Doppler shift relation

$$\sigma^2 = gk \tanh(kh) \quad (2)$$

$$\sigma = \omega - \vec{k} \cdot \vec{U} \quad (3)$$

where h is the water depth relative to mean water level, ω is the apparent frequency, \vec{k} is the wave number vector taking into account the direction of wave propagation. The phase velocity C and the group velocity C_g are defined as

$$C = \sigma/k; \quad C_g = \partial \sigma / \partial k \quad (4)$$

In order to better simulate nonlinear waves in shallow waters, an alternative to (3) is the amplitude-dependent dispersion relation developed by Kirby and Dalrymple (1986)

$$\sigma^2 = gk(1 + (kA)^2 F_1 \tanh(kh)) \tanh(kh + kAF_2) \quad (5)$$

where A is the wave amplitude and

$$F_1 = \frac{\cosh(4kh) + 8 - 2 \tanh^2(kh)}{8 \cosh^4(kh)}; \quad F_2 = \left(\frac{kh}{\sinh(kh)} \right)^4 \quad (5a)$$

For practical applications, wave breaking is an important mechanism, which may be induced by both shallow depths and strong opposing currents. A dissipation term, is therefore, added to the model Eq. (1) which yields (Booij, 1981; Liu, 1990)

$$\frac{D^2 \Phi}{Dt^2} + (\nabla \cdot \vec{U}) \frac{D\Phi}{Dt} - \nabla \cdot (CC_g \nabla \Phi) - (k^2 CC_g - \sigma^2 + i\sigma W) \Phi = 0 \quad (6)$$

where W , a parameter associated with wave breaking and bottom friction, is a function of the (unknown) wave height.

For monochromatic waves, the wave potential can be expressed as

$$\Phi(x, y, t) = \phi(x, y) \exp(-i\omega t) \quad (7)$$

Substituting (7) into (6) gives

$$\begin{aligned} \nabla \cdot (CC_g \nabla \phi) - \nabla \cdot (\vec{U} (\vec{U} \cdot \nabla \phi)) + 2i\omega \vec{U} \cdot \nabla \phi \\ + (k^2 CC_g + \omega^2 - \sigma^2 + i\omega \nabla \cdot \vec{U} + i\sigma W) \phi = 0 \end{aligned} \quad (8)$$

Kostense et al. (1988) and Li and Anastasiou (1992) have dropped the second term in (8) under the assumption that this term is small compared to the first one. Since solving this term takes very little extra computational effort in a finite element approach, for generality we have retained the full version of (8) as our governing equation.

The relation between surface elevation and wave potential may be obtained from the surface boundary condition as

$$\eta = \frac{1}{g} \left(i\omega + \vec{U} \cdot \frac{\nabla \phi}{\phi} \right) \phi \quad (9)$$

and further simplification of (9) gives the following linear relation which is more commonly used (Liu, 1983; Kirby, 1984),

$$\eta = \frac{i\sigma}{g} \phi \quad (10)$$

Eq. (10) assumes that wave amplitude gradient ($\nabla|\phi|/|\phi|$) is small in the direction of the current compared to the phase gradient $\nabla(\arg \phi)$. The assumption is true only if the back-scattered and reflected waves are relatively weak compared to the incident waves.

3. Boundary conditions

Eq. (8) is elliptic and requires boundary conditions along both physical boundaries (i.e. shorelines and structures) and open boundaries (i.e. artificial water boundaries). A physical boundary, characterized by a pre-specified reflection coefficient, can either partially or

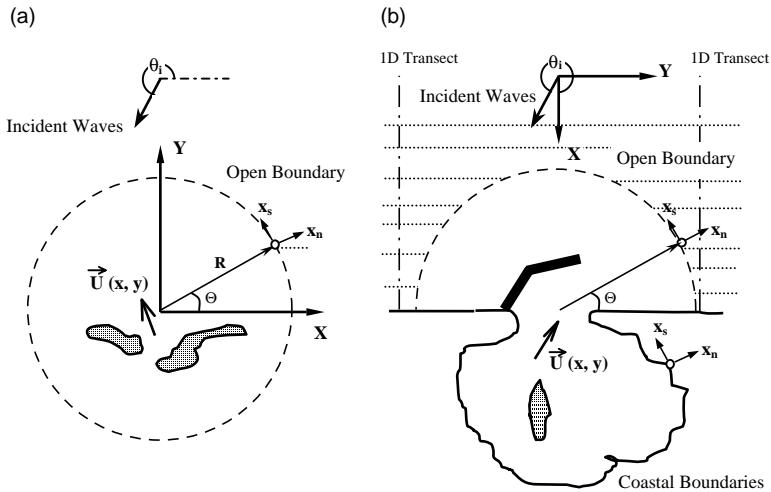


Fig. 1. Definition sketch of model domain. (a) Open sea application; (b) coastal/harbor application.

fully reflect or fully absorb approaching waves, while an open boundary is always intended to be fully transmitting to both outgoing and incoming waves. As shown in Fig. 1, an application may be classified as either an open-sea application that uses a full-circle open boundary, or as a coastal/harbor application for which a semicircle open boundary is more appropriate. Circular arcs are favored for open boundaries since the directions of scattered waves are more likely to be perpendicular to the boundary. Detailed descriptions of boundary conditions for both application types are presented below.

3.1. Open sea problems

The wave potential ϕ at an open boundary may be divided into a pre-determined part ϕ_0 , and an unknown part ϕ_s that represents the scattered wave field. For an open sea problem, it is assumed that the bathymetric change and ambient currents outside the modeling domain are small and have no significant effect on incident waves. As such, ϕ_0 can be specified as the incident wave condition in a plane-wave form

$$\phi_0 = (-ig/\sigma)A_i \exp[ikR \cos(\Theta - \theta_i)] \quad (11)$$

where R is the radius of the open boundary circle, (R, Θ) denotes a node location on the boundary in polar coordinates (Fig. 1a), A_i and θ_i are the surface amplitude and angle of the monochromatic incident waves. ϕ_s represents the effect of non-homogeneities and is induced by currents, bathymetric variations, and physical boundary reflections within the modeling domain; to describe this, a parabolic-type absorbing boundary condition may be used (Xu et al., 1996; Kirby, 1989),

$$\frac{\partial \phi_s}{\partial x_n} = p\phi_s + q \frac{\partial^2 \phi_s}{\partial x_s^2} \quad (12)$$

where (x_n, x_s) denotes a local coordinate system with x_n normal (in the radial direction) and x_s tangential to the boundary, p and q are two known functions which, following Xu et al. (1996), may be written in the polar coordinate system as

$$p = ik - \frac{1}{2R} + \frac{i}{8kR^2}; \quad q = \frac{i}{2k} \quad (13)$$

By combining the conditions for ϕ_0 and ϕ_s , the open boundary condition for ϕ becomes

$$\frac{\partial \phi}{\partial x_n} = p\phi + q \frac{\partial^2 \phi}{\partial x_s^2} + g \quad (14)$$

where

$$g = \frac{\partial \phi_0}{\partial x_n} - p\phi_0 - q \frac{\partial^2 \phi_0}{\partial x_s^2} \quad (14a)$$

Any physical boundary that lies within the modeling domain may be fully or partially reflective; a general boundary condition may be written as

$$\frac{\partial \phi}{\partial x_n} = \left(ik \cos \gamma \frac{1 - K_r \exp(ik\beta)}{1 + K_r \exp(ik\beta)} + \frac{1}{A_I} \frac{\partial A_I}{\partial x_n} \right) \phi \quad (15)$$

where K_r is the reflection coefficient, β is the phase shift between incident and reflected waves at the boundary, γ is the incident wave angle relative to the normal direction (x_n) of the coastal boundary, and A_I is the amplitude of the incident waves approaching the boundary. The first term of (15) was initially derived by Isaacson and Qu (1990), taking into account the partial boundary reflection for waves incident at an arbitrary angle; the second term, derived by Chen et al. (2002), accounts for the wave height gradient at the boundary. The second term may be estimated from the linear wave ray theory (energy conservation) as

$$\frac{1}{A_I} \frac{\partial A_I}{\partial x_n} \cong -\frac{1}{2} \frac{\partial \theta}{\partial x_s} - \frac{1}{2C_g} \frac{\partial C_g}{\partial x_n} \quad (15a)$$

where as shown in Fig. 2, θ is the approaching wave direction accounting for both wave incident angle γ and boundary orientation angle Θ , such that $\theta = \Theta + \gamma$. The two terms on the right-hand side of (15a) represent, respectively, the effects of wave convergence or divergence and bathymetric change. It is noted that (15a) does not account for the energy dissipation, and so it is invalid if waves were to break before reaching the boundary (shoreline). In that event, though, (15a) becomes insignificant and can simply be neglected.

Eq. (15) is nonlinear in the sense that the wave angle γ is a function of the unknown ϕ . Most conventional wave models have in practice neglected the outgoing wave angle by setting $\gamma = 0$. This often results in spurious effects, while simulating wave transformation in harbors or jettied inlets (Isaacson and Qu, 1990; Beltrami et al., 2001; Chen et al., 2002). Further, as demonstrated by Chen et al. (2002), (15a) eliminates spurious reflections arising from boundary curvature and the depth cut-off at shoreline boundaries (since zero depth is not allowed). The boundary condition (15) can, therefore, overcome

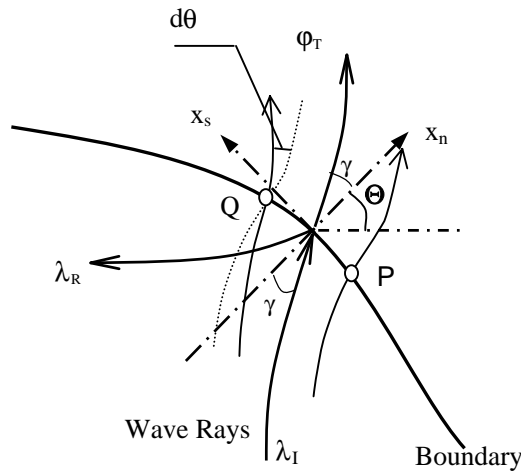


Fig. 2. Outgoing wave rays at a boundary.

the limitations of more approximate forms traditionally used (e.g. see Panchang and Demirebilek (2001) for a review).

3.2. Coastal and harbor problems

The semi-circular open boundary used for coastal and harbor problems (Fig. 1b) is comparatively more difficult to deal with, primarily because of nearshore bathymetric change and ambient currents in the exterior of the semicircular boundary. In this case, the wave potential ϕ_0 , which may include both incident waves and reflected waves in the exterior, will be affected by the exterior bathymetry and currents, it therefore, no longer remains in the form of simple plane waves.

The difficulties resulting from the exterior bathymetry can be partly overcome by introducing a one-dimensional (referred to as 1D, hereafter) model for ϕ_0 to properly account for the effect of the exterior bathymetry (Panchang et al., 2000). The 1D model rests on the assumption that exterior depth varies only in the cross-shore direction (Fig. 1b). Together with the approximation of $\vec{k} \cong \nabla(\arg \phi_0)$ which leads to Snell's Law ($k_y = k_0 \sin \theta_i = \text{constant}$), we obtain the following 1D form of the mild-slope equation and the boundary conditions

$$\frac{d}{dx} \left(CC_g \frac{d\psi}{dx} \right) + ((k^2 - k_y^2)CC_g + i\sigma W)\psi = 0 \quad (16)$$

$$\frac{d\psi}{dx} = ik \cos \theta_i \left(-\frac{ig}{\sigma} 2A_i - \psi \right) \quad x = 0 \text{ at offshore} \quad (17)$$

$$\frac{d\psi}{dx} = \left(i\sqrt{k^2 - k_y^2} \frac{1 - K_r \exp(ik\beta)}{1 + K_r \exp(ik\beta)} + \frac{1}{A_I} \frac{dA_I}{dx} \right) \psi \quad x \text{ at shoreline} \quad (18)$$

where the second term in (18) may be neglected if wave breaking occurs, before waves reach the boundary, otherwise it is given by

$$\frac{1}{A_I} \frac{\partial A_I}{\partial x} = -\frac{1}{2C_g} \frac{\partial C_g}{\partial x} \quad (18a)$$

In Eqs. (16)–(18), the variable ψ is related to ϕ_0 by

$$\phi_0 = \psi(x)\exp(ik_y y) \quad (19)$$

where (x, y) refers to a coordinate system shown in Fig. 1b, with the incident wave condition specified at the origin, the offshore end of the 1D transect.

In practical applications, two 1D solutions ψ_1 and ψ_2 may be sought to account for the bathymetry differences between two sides of the semicircular open boundary. To obtain ϕ_0 along the boundary, the two solutions are further interpolated and mapped onto the boundary as

$$\phi_0 = \left(\frac{1+y/R}{2} \psi_1(x) + \frac{1-y/R}{2} \psi_2(x) \right) \exp(ik_y y) \quad (20)$$

where R is the radius of the semicircular boundary.

While the above treatment has been shown to effectively handle the problem of the bathymetric variations in the exterior (Panchang et al., 2000; Zhao et al., 2000; Panchang and Demirbilek, 2001), the problem of varying ambient currents in the exterior is more challenging and has no standard solution yet. If the current field were to vary only in the x (cross-shore) direction in the exterior, i.e. $\vec{U} = (u(x), v(x))$, its effect may be incorporated into the 1D model for the solution of ϕ_0 . However, such a current field is rare in practice and we perforce assume that the effect of ambient currents on incident waves is negligible in the exterior region. Diligence should be exercised in selecting the model domain and in specifying ϕ_0 .

For the scattered waves, depth variations that occur along the semicircular boundary may render the parabolic condition (12) inappropriate (Panchang et al., 2000); a simple expression for q as in (13) cannot be obtained. In such a case, the lower-order absorbing boundary condition (15) that incorporates the incident angle would be more applicable. Because the open boundary is fully transmitting ($K_r=0$), ϕ_s along this boundary may be written as

$$\frac{\partial \phi_s}{\partial x_n} = \left(ik \cos \gamma - \frac{\partial \theta}{2 \partial x_s} - \frac{1}{2C_g} \frac{\partial C_g}{\partial x_n} \right) \phi_s \quad (21)$$

It is noted that, in cases, where the bottom slope is mild and scatterers are weak and originate from near the center of a large semicircle, (21) can be effectively simplified as

$$\frac{\partial \phi_s}{\partial x_n} = \left(ik - \frac{1}{2R} \right) \phi_s \quad (22)$$

which is the same form used by Panchang et al. (2000).

The overall open boundary condition for ϕ is then

$$\frac{\partial \phi}{\partial x_n} = \left(ik - \frac{1}{2R} \right) (\phi - \phi_0) + \frac{\partial \phi_0}{\partial x_n} \quad (23)$$

where quantities related to ϕ_0 are obtained from (19) or (20).

The coastal boundary condition for coastal/harbor problems is the same as that for open sea problems, and is given by (15).

4. Numerical implementation

Eq. (8) together with the dispersion relations and the appropriate boundary conditions as described above forms a formidable boundary value problem from the viewpoint of numerical implementation. Nonlinearities are encountered in the governing equations (wave–current interaction and wave breaking) and in the boundary conditions (when the direction-related expressions are employed). Nonlinear mechanisms can only be treated in an iterative manner, allowing the boundary value problem to be linearized and solved during each iteration by means of the finite-element method. Three aspects of the numerical implementation are discussed below.

4.1. Determination of nonlinear parameters

4.1.1. Wave direction and Doppler shift

The effect of current-induced Doppler shift is incorporated into the kinematic parameters k and σ through the combined dispersion relations (2) and (3) or (5) and (3). To determine the parameters k and σ , it is necessary to first calculate the wave direction. Wave direction is traditionally obtained from the phase gradient, which is

$$\nabla(\arg \phi) = \nabla(\text{Im}(\ln \phi)) = \text{Im}(\nabla \phi / \phi) \quad (24)$$

therefore, the wave direction θ is determined by,

$$\tan \theta = \frac{\frac{\partial(\arg \phi)}{\partial y}}{\frac{\partial(\arg \phi)}{\partial x}} = \text{Im} \left(\frac{1}{\phi} \frac{\partial \phi}{\partial y} \right) / \text{Im} \left(\frac{1}{\phi} \frac{\partial \phi}{\partial x} \right) \quad (25)$$

Taking θ as the direction of vector \vec{k} , the Doppler shift relation (3) can then be re-written as

$$\sigma = \omega - k(u \cos \theta + v \sin \theta) \quad (26)$$

Once θ is known the intrinsic frequency σ and the Doppler shifted wave number k may be obtained by solving the combined nonlinear Eqs. (2) and (26), or (5) and (26) if one uses the nonlinear dispersion relation.

It is noted that wave direction can be defined only in a wave field that is mainly progressive. In some harbor areas, the wave field ϕ may contain multi-directional wave components due to wave scattering and reflection. The wave direction obtained from (25) may then be viewed as the primary direction of wave propagation. Since the parameters

k and σ are calculated on the basis of this wave direction, the effect of currents (Doppler shift) on scattered waves moving in other directions cannot be correctly accounted for by using these parameters. Strictly speaking, in a combined wave–current environment, wave kinematics and the flowfield dynamics are coupled and cannot be solved separately. If the wave field is dominated by waves that have readily identifiable directions, the effect of currents on other (weak) wave components would remain small so as not to significantly affect the accuracy of modeling results. This is true because the scattered field is generally weak when there is no significant wave reflection from coastal boundaries. In case of strong coastal reflection, we have to assume that reflected waves do not ride through the major current field in directions largely collinear with flow directions. Otherwise the reflected wave field must be treated separately from the forward-propagating wave field. This aspect remains a topic of further research.

4.1.2. Outgoing wave angle at a boundary

The absorbing boundary conditions (15) and (21) require knowledge of γ , the incident wave angle relative to the normal direction at the boundary. For scattered waves at the offshore open boundary, this angle can be determined in a manner similar to (25) with

$$\tan \gamma = \frac{\partial(\arg \phi_s)}{\partial x_s} \bigg/ \frac{\partial(\arg \phi_s)}{\partial x_n} \quad (27)$$

At a coastal boundary, however, as noted in Section 3, approaching waves may be partially reflected. In the presence of reflected waves, (25) cannot be used to find γ because of the multi-directionality in the wave potential ϕ . Considering the combination of incident and reflected waves, Chen et al. (2002) and Steward and Panchang (2001) have developed the following equation for determining the approaching wave direction and demonstrated its robustness for use in nonlinear calculations,

$$\tan \gamma = \frac{(1 - K_r^2)}{1 + 2K_r \cos(k\beta) + K_r^2} \frac{\partial(\arg \phi)}{\partial x_s} \bigg/ \frac{\partial(\arg \phi)}{\partial x_n} \quad (28)$$

Note that (28) reverts to (27) when boundary has zero reflection ($K_r=0$), and (27) reverts to (25) if x and y were used instead of x_n and x_s . (28) may present difficulties when $\partial(\arg \phi)/\partial x_n$ and $\partial(\arg \phi)/\partial x_s$ are both nearly zero. This implies a situation with standing waves, which eliminates the need for an establishing γ for use in (15).

4.1.3. Breaking parameter W

A number of formulations for the wave breaking parameter W can be found in the literature, but few of them have been well-tested in an environment with strong wave–current interaction. In the absence of wave–current interaction, Zhao et al. (2000) examined five different parameterizations for W and concluded that the formulations of Battjes and Janssen (1978) and Dally et al. (1985) are the most robust for use with the mild-slope wave equation. Later, Zubier et al. (2003) indicated that the formulation of Battjes and Janssen (1978) provides a better fit to field data than that of Dally et al. (1985). We therefore use, in this work, the breaking criterion of Battjes and Janssen (1978), which has also been used by Booij et al. (1999) in their energy-balance wave model.

4.2. Finite element formulation and solution of linear systems

The flexibility afforded by the choice of finite elements not only permits the best fit to arbitrarily-shaped boundaries, but also provides the most efficiency in grid generation. Locally wavelength-dependent grids (with a typical resolution of 15–20 grids per wavelength) of varying size can be used, hence keeping the number of grids to an optimum. (The finite-difference method, on the other hand, requires an excessive number of grids since the size would be limited based on the shallowest depths; this compounds the computational difficulties). We used a graphics software package called the Surface Water Modeling System (Zundel et al., 1998) to construct a network of triangular finite elements.

With the inclusion of wave–current interaction, the governing Eq. (8) becomes more complicated, requiring in the finite-element formulation use of the more general variational principle (Galerkin approach), rather than the Jacobian functional method used by Xu et al. (1996). For each of the n nodes in the discretized domain, a linear weighting function is chosen on basis of local triangular meshes. Integration of (8) in accordance with the Galerkin principle leads to a large sparse linear system

$$[\mathbf{K}]\{\phi\} = \{f\} \quad (29)$$

where $[\mathbf{K}]$ is the $n \times n$ stiffness matrix, $\{f\}$ the load vector, and $\{\phi\}$ the solution vector of unknowns ϕ_i ($i=1,2,\dots,n$). Details of derivation may be found in Chen, 2002).

As in the case without ambient current, (29) forms an extremely large (n is typically at an order of 10^5) complex-valued system. Without ambient currents, Panchang et al. (1991) solved (29) by applying a pre-conditioned conjugate gradient iterative scheme to the normalized equation. Several other iterative methods have since been used with varying success (Li, 1994; Oliveira and Anastasiou, 1998). The iterative scheme of Li (1994) is probably the most efficient algorithm for solving the symmetric linear system resulting from the mild-slope equation or its variants without currents. However, when currents are included, the stiffness matrix $[\mathbf{K}]$ is no longer symmetric or Hermitian, as a result of the additional term $\vec{U} \cdot \nabla \phi$ in (8). We found that Li's algorithm then does not lead to convergence. Even the stabilized biconjugate method (BiCGStab, Van der Vorst, 1992), originally developed for solving nonsymmetric systems, failed to yield a converged solution for some of the test cases presented in the next section. It is concluded based on our testing that, for a nonsymmetric and non-Hermitian complex-valued linear system associated with (8), the algorithm of Panchang et al. (1991) is probably the most robust and guaranteed to converge.

4.3. Iterative scheme for multiple nonlinear mechanisms

As noted earlier, the parameters k , σ , W and γ are nonlinear and have to be solved, together with ϕ , by iteration. In an iterative scheme, these nonlinear parameters are pre-determined based on the solution of ϕ from the previous iteration step, so that a new linear system for ϕ can be formed based on the finite-element method and solved as discussed above. The first linear solution ϕ may be obtained by assuming zero currents ($U=0$), no breaking ($W=0$), and $\gamma=0$. The nonlinear iterations proceed until the following stopping

criterion is met:

$$\text{Maximum}_{i=1,n} ||\phi_i|_j - |\phi_i|_{j-1}|/|\phi_{\text{inc}}| < \varepsilon \quad (30)$$

where i is the node number, j the number of iterations, $|\phi_{\text{inc}}|$ the amplitude of the incident wave potential at offshore ($x=0$), and ε is a pre-specified tolerance (typically $\varepsilon=10^{-3}$). Since $|\phi_{\text{inc}}|$ is a fixed reference value for all nodes, (30) actually defines the maximum tolerable absolute error (solution difference between two successive iterations) for the entire domain.

The behavior of solution convergence is highly case-dependent, so termination may require some judgment in adjusting the tolerance level ε , or even the use of different stopping criteria. In iterative methods, a very common approach is to use a relative error (either maximum or average) for checking convergence. However, we found that using the relative error imposed unnecessarily high accuracy on smaller waves in the breaking zone while trying to maintain the desirable accuracy in the more prevalent non-breaking area. Due to the dissipation term, iterative solutions in the breaking zone are more likely to remain oscillating with small amplitudes, which could prevent convergence/model termination. Our analysis indicated that using absolute error in the stopping criterion, as given in (30), helps faster convergence without sacrificing the accuracy of solution in the higher wave zones. It appears that (30) is a robust stopping criterion, capable of identifying a reliable solution in general.

Iterative methods have been used for nonlinear mechanisms such as wave breaking (De Girolamo et al., 1988; Zhao et al., 2000), wave direction-dependent boundary conditions (Isaacson and Qu, 1990; Steward and Panchang, 2001; Beltrami et al., 2001), and wave–current interaction (Kostense et al., 1988). There has been a concern that multiple nonlinear mechanisms could slow down or even impede solution convergence. Our study shows that multiple nonlinear parameters may be updated and iterated simultaneously without difficulties in achieving convergence. This indicates that highly nonlinear wave–current interaction problems can be solved effectively in such a manner.

5. Model validation

In this section, three cases of wave–current interaction of common interest are simulated using the methods described above. The absence of data or analytical solutions for typical cases of two-dimensional wave–current interaction precludes model validation in the usual sense; however, the results are evaluated for overall consistency by comparing them to the results of other models (either parabolic or Boussinesq time-dependent finite-difference models).

5.1. Vortex ring

Vortex rings, commonly seen in open oceans and coastal seas, have important effects on marine physical and biological processes (e.g. Mapp et al., 1985; Liu et al., 1994). The complex wave patterns resulting from wave and vortex interaction can be captured by

airborne or satellite imagery. Liu et al. (1994) combined image processing and simple wave modeling to identify the existence and strengths of underlying vortex rings. The modeling procedure described here can be used as a more sophisticated alternative in future studies of vortical flows and ocean gyres. Although this case can be easily tackled using simpler parabolic approximation models, we describe it here for two reasons: (a) to validate the code we developed before applying it to other cases, and (b) to highlight certain features of the wave pattern that occur in more practical harbor engineering problems discussed later (Section 6).

We consider the case of wave-vortex interaction studied by Mapp et al. (1985) and Yoon and Liu (1989), who describe the current field as

$$V_r = 0$$

$$V_\theta = \begin{cases} C_5 \left(\frac{r}{R_1} \right)^N & r \leq R_1 \\ C_6 \exp \left[- \left(\frac{R_2 - r}{R_3} \right)^2 \right] & r \geq R_1 \end{cases} \quad (31)$$

where V_r and V_θ are the velocity components in polar coordinates with the origin at the center of the ring. Following Yoon and Liu (1989), we set

$$C_5 = 0.9 \text{ m/s}; \quad C_6 = 1.0 \text{ m/s}; \quad N = 2; \quad R_1 = 343.706 \text{ m};$$

$$R_2 = 384.881 \text{ m}; \quad R_3 = 126.830 \text{ m}. \quad (32)$$

Such a vortex ring creates a shearing current (maximum $V_\theta = 1 \text{ m/s}$) all around the circle. Since the water depth is constant ($h = 10 \text{ m}$), we choose a circular computational domain (of radius $R = 1800 \text{ m}$) using the boundary conditions described in Section 3.1. This case provides a perfect test for pure wave–current interaction, in which plane waves (with an incident amplitude of $A_i = 1 \text{ m}$ and period $T = 19.43 \text{ s}$) meet currents at all angles. As shown in Fig. 3a, the vortex ring is centered at $(x_0, y_0) = (0, 1000 \text{ m})$. The domain is evenly discretized into triangular meshes with about 20 nodes per wavelength, generating a total of 102,171 nodes. The simulation starts with a plane wave solution and convergence

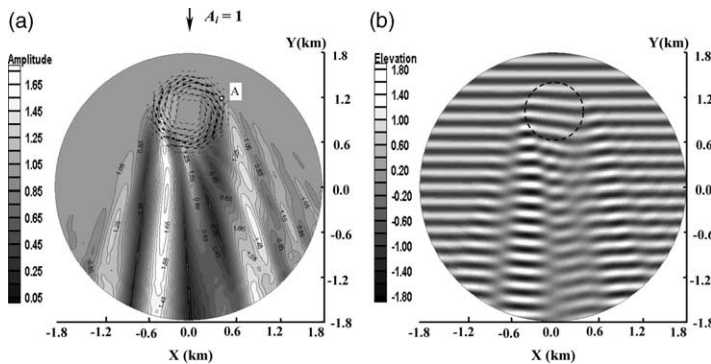


Fig. 3. Model results for wave–vortex ring interaction. (a) Amplitude; (b) surface elevation.

is reached after only four nonlinear iterations for wave–current interaction. Wave breaking is not activated in this case. The total run time for this simulation is about 15 min on a 2.4 GHz desktop PC.

The simulated wave amplitude and a snapshot of the surface elevation are presented in Fig. 3. As can be seen, wave energy has been considerably redistributed due to the disturbance created by the vortex ring. The effect of vortical flow on wave propagation is complicated because progressive waves encounter shear currents at all angles. The vortex ring not only affects the area, where opposing (left-hand side) and following (right-hand side) currents exist, but also a large part of the down-wave region. The combined effect of wave refraction, diffraction, and reflection give rise to modulations of wave amplitude that are neither symmetric nor regularly oriented.

Yoon and Liu (1989) modeled this problem with a finite-difference, phase-resolving, parabolic approximation. The overall wave pattern obtained by them (Fig. 13a in Yoon and Liu, 1989) is similar to ours (Fig. 3a and b). Fig. 4 provides a detailed quantitative comparison of the two model results for six lateral transects. Although the two models agree well for this test case, it is noted that the method presented here has greater versatility because it does not rely on the parabolic approximation. In fact, some limitations of the parabolic approximation may be captured in Figs. 3 and 4. For instance, due to the highly oblique angle with which waves approach the shearing current in the vicinity of point A in Fig. 3a, wave caustics are expected to occur, causing a small band of waves to be reflected toward the right (McKee, 1974; Peregrine and Smith, 1975). The reflection is manifested in the form of amplitude modulations in our results (e.g. down-wave and to the right of point A in Fig. 3, and to the right of B and C in Fig. 4). The parabolic approximation model is not expected to simulate wave reflection or large-angle diffraction, hence the model results of Yoon and Liu (1989) show a less disturbed solution

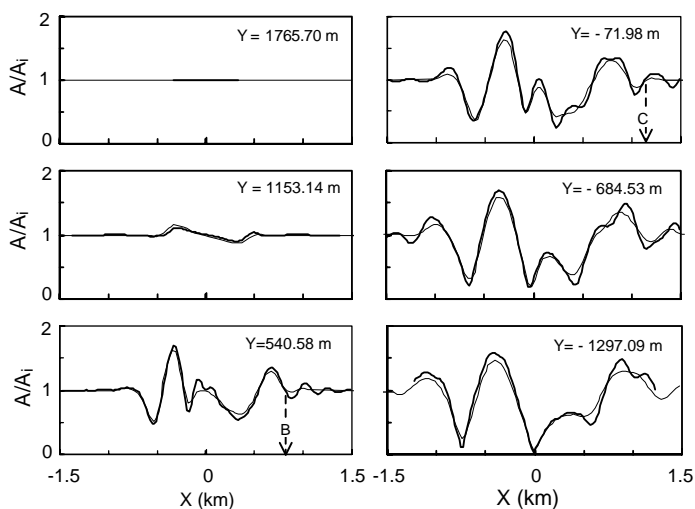


Fig. 4. Simulated relative wave amplitudes for wave–vortex ring interaction (thick line: present model; thin line: Yoon and Liu (1989)).

to the right of B and C in Fig. 4. This type of reflection of waves that are obliquely incident on a shearing current is relevant to our simulations pertaining to the interaction of waves with tidal currents near an inlet (see Section 6.4).

5.2. Rip current on sloping beach

Wave-induced rip currents play a significant role in nearshore morphodynamics. Waves propagating over a rip current system on a sloping beach experience both bathymetric shoaling and current-induced refraction-diffraction. For an idealized case, the interaction of a rip current and shoaling waves was originally studied by Arthur (1950) using a linear geometric ray model. The problem considered has a sloping beach with a uniform slope of 1/50. The current field based on a local coordinate system (shown in Fig. 5) is given by

$$\begin{aligned} u &= 0.1442yF\left(\frac{x}{7.62}\right)F\left(\frac{y}{76.2}\right); \\ v &= -0.5192\left[2 - \left(\frac{y}{76.2}\right)^2\right]F\left(\frac{y}{76.2}\right)\int_0^{x/7.62} F(\tau)d\tau \end{aligned} \quad (33)$$

with

$$F(\tau) = \frac{1}{\sqrt{2\pi}} \exp\left(-\frac{\tau^2}{2}\right) \quad (34)$$

In accordance with the boundary formulation described in Section 3.2, we use a semicircular domain (of radius $R=240$ m and containing over 85,000 nodes), for which currents far away from the center of the domain have no cross-shore component and hence no effect on normally incident waves. A normally incident wave of unit amplitude is specified at a distance of 240 m offshore. (For greater clarity, only a portion of the complete semicircular domain is shown in Fig. 5 and others like it). The incoming wave potential ϕ_0 along the open boundary is obtained by solving the 1D model as described by Eqs. (16)–(18) and is

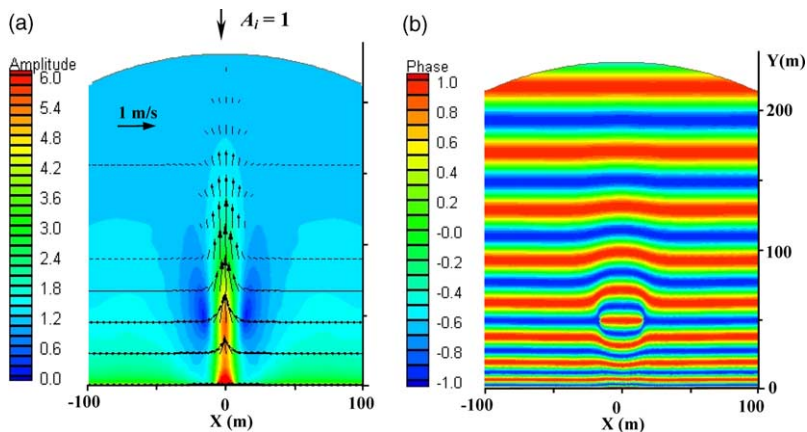


Fig. 5. Modeled wave field in the presence of a rip current. (a) Amplitude; (b) phase.

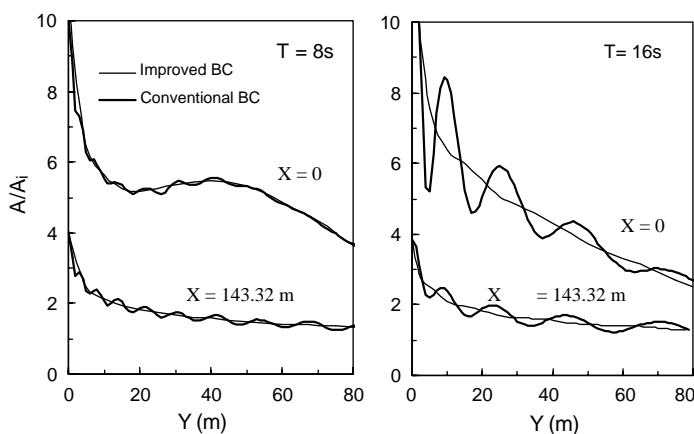


Fig. 6. Simulated relative wave amplitudes using two boundary conditions.

substituted into (23) to obtain the open boundary condition for the 2D model. Wave breaking is not activated for consistency with other model results (e.g. Yoon and Liu, 1989).

To avoid the singularity of zero depth at the coastline, we place the shoreline boundary at $y=1$ m, where the cut-off depth is 0.02 m; it is specified as non-reflective boundary ($K_r=0$, $\beta=0$) using generalized boundary condition (15). Because of the large shoaling effect near the shoreline, the second term in (15) plays an important role. This can be seen in Fig. 6, where results for simulations with two different incident wave periods are shown. The improved boundary condition (15) is effective in eliminating spurious reflections resulting from the cut-off depth at the shoreline. These spurious reflections are seen quite significant for longer waves, even with a very mild bottom slope (1/50) in this case.

The model simulation for $T=8$ s in this case took five nonlinear iterations and about 10 min. Results shown in Fig. 5 indicate that the opposing rip current has modified the wavelengths and caused a notable bending of phase contours. As a consequence, wave energy is focused and trapped to form a high-wave zone along the centerline across shore; this is accompanied by two symmetric shadow regions on the sides. The combined effects of the rip current and bathymetric shoaling cause amplitude amplification to a factor over six in the central area.

Our results are compared in Fig. 7 to the parabolic approximation results of Yoon and Liu (1989) along four longshore and two cross-shore transects, and again fairly good agreement is seen in general. However, there is an obvious mismatch along $x=0$ for $y<60$ m. Our results show that the amplitude has a peak value of 5.5 at approximately 45 m offshore, and after a small drop, it increases to about 10 at the boundary. In other words, the non-breaking amplitude has nearly doubled in the shallowest 25 m of the domain, where opposing current is becoming negligible. The results of Yoon and Liu (1989), on the other hand, show a significant drop from the peak value of 5 down to 3.2. While using a different parabolic approximation, Liu (1983) speculated that this amplitude drop was related to the lateral component of the current. We investigated this with the elliptic finite-element model and found that suppressing the lateral velocity u made

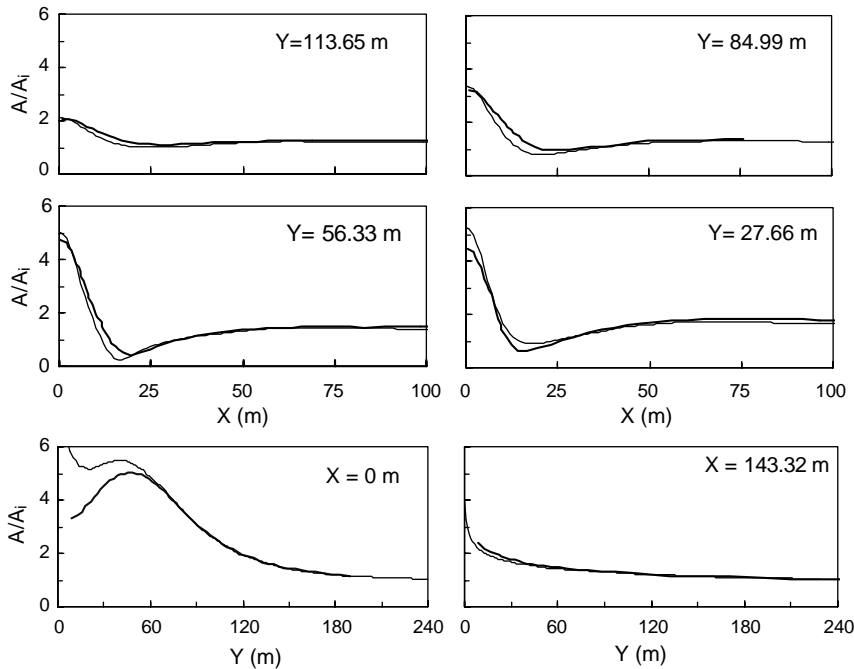


Fig. 7. Simulated relative wave amplitudes, rip current case (thick line: present model; thin line: Yoon and Liu, 1989).

little difference. On the other hand, it may be noted that shoaling alone causes a similar doubling at other cross-shore transects (e.g. $x = 143.34$ m). We submit, therefore, that the increase in the amplification obtained by the elliptic model is a reasonable feature that the parabolic approximation cannot capture. Parabolic approximations assume that the second derivative of wave amplitude in the dominant wave propagation direction is of higher-order and hence dropped; in this case, the assumption may not be appropriate. The mismatch between the parabolic approximations and elliptic equation solutions (Fig. 7) are significant only near the central nearshore area or around the shadow areas ($x \cong \pm 15$ m), where wave amplitudes apparently experience considerable change in the x direction. At distant cross-shore sections, the two models agree because changes in the x -direction are less enhanced.

5.3. Rip current on beach with sandbar

We consider a second, more realistic, rip current case that has been studied by Chen et al. (1999). Fig. 8 shows the bathymetry of a plane beach with a discontinuous offshore sandbar and the underlying rip current field. The current field, provided to us by Professor Q. Chen of the University of South Alabama, is more complicated than that in Section 5.2. Strong vorticity characterizes much of the current field, for instance, on both sides of the central jet of the rip current and also behind the sandbar in the surf zone. The vortices

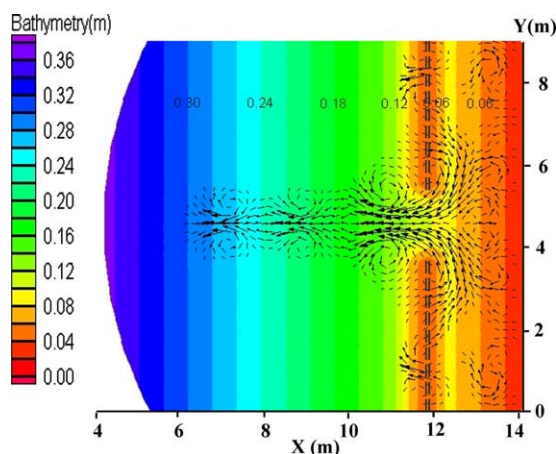


Fig. 8. Plane beach with gapped sandbar (following Chen et al., 1999) bathymetry and the underlying rip current (double-dashed lines indicate sandbar locations).

have spatial scales comparable to the wavelengths, indicating large velocity gradients. In this case, the semicircular computational domain ($R=10$ m) contains 75,871 nodes. A normally incident wave train with period $T=1$ s and amplitude $A_i=0.024$ m is prescribed at 10 m offshore, and the coastal boundary, specified as fully absorbing, is placed at a cut-off depth of 0.03 m. Nonlinear iterations are performed simultaneously for all nonlinear mechanisms, including wave breaking. In general, the number of nonlinear iterations required is greater when the breaking mechanism is activated. This case required 13 iterations to reach convergence, but the total run time is only about 8.4 min.

The results of the simulated wave field are shown in Fig. 9. The snapshot of the surface wave elevation (Fig. 9a) reveals a complex wave pattern due to the combined effects of varying bathymetry and underlying rip current. This wave pattern is visually similar to those obtained by Chen et al. (1999, Plate 6) using a modified Boussinesq model (Wei et al., 1995; Chen et al., 2000; Kennedy et al., 1998). The resulting amplitude and phase diagrams (Fig. 9b and c) are understandably complex. It is clear, though, that along the centerline large-waves build up and then break right in front of the gap, at a depth of approximately 0.12 m. Away from the central channel, the breaking line is largely along the toe of the underwater sandbar. Behind the bar, waves appear to be disturbed by the vortical flow, which results in fluctuating phase lines indicating short-crestedness (Fig. 9a and c).

Fig. 10 shows the quantitative comparison of our model results to those from the time-dependent Boussinesq model of Chen et al. (1999) along the central cross-shore transect. The surface elevation from two model simulations agrees reasonably well (Fig. 10a). Minor differences are possibly due to the nonlinear shallow water effects (wave–wave interaction) that are not included in (8). The Boussinesq model surface elevations show sharp crests and wide troughs in the surf zone (Fig. 10a), indicating the importance of the nonlinearities in the shallow water areas. This results in a phase offset between the two modeled water surface elevations in the shallow region. The accumulated phase offset increases in the shoreward direction. Panchang and Demirbilek (2001) describe the finite

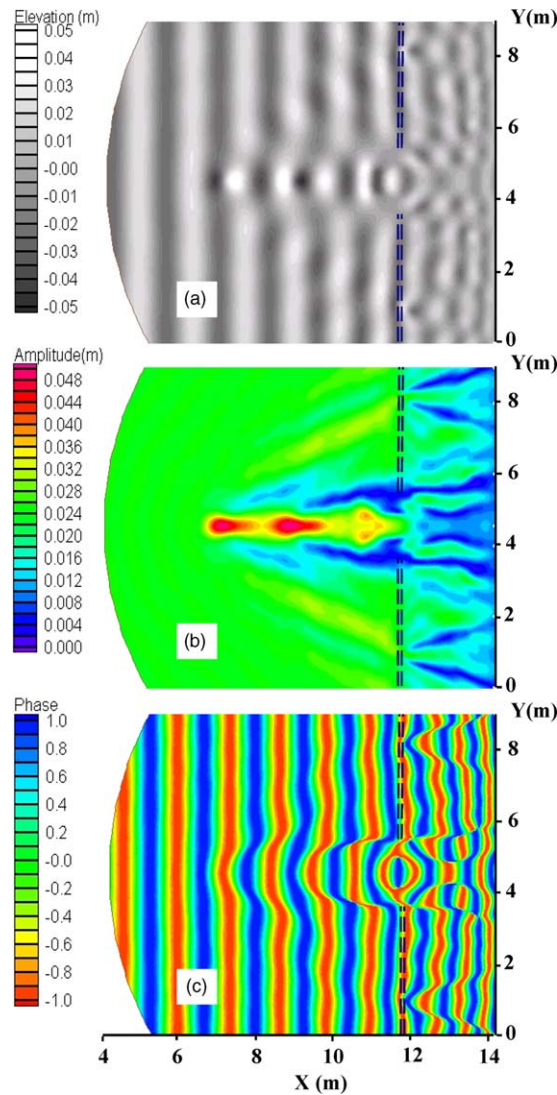


Fig. 9. Model results for the rip current case of Chen et al. (1999). (a) Surface elevation; (b) amplitude; (c) phase.

element modeling of (8) when wave–wave interactions are included; however, the combination of wave–wave interaction and wave–current interaction has not yet been reported. Nevertheless, we have found that incorporating nonlinear dispersion relation (5) can partially remedy this situation. This is shown in Fig. 10 (bottom panel), where the phase offset has been largely eliminated. Discrepancies in Fig. 10 may also be attributed to differences in the implementation of wave breaking in the models. The amplitude distribution predicted by the present model (shown as a dotted curve in Fig. 10a) identifies the breaking point to be at $x \approx 11.2$ m, while results from the Boussinesq model show wave

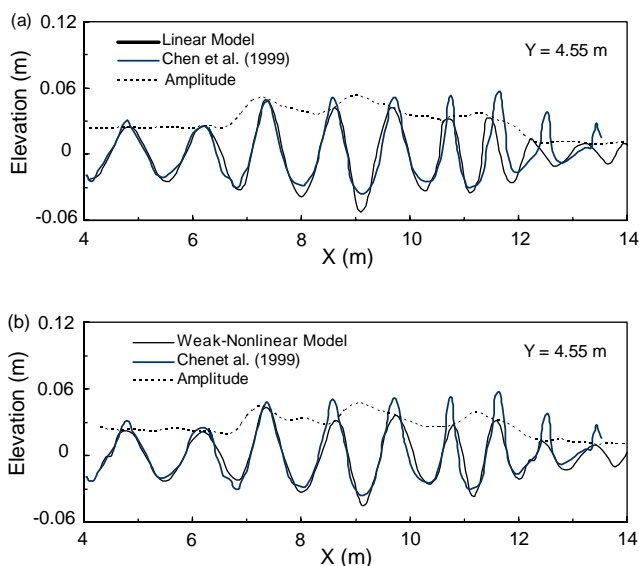


Fig. 10. Simulations of the rip current case of Chen et al. (1999).

heights decreasing only after $x \cong 12$ m. The absence of benchmark data is a handicap preventing us from further verifying the breaking criteria used the two models.

6. Wave pattern near a jettied tidal inlet

The effect of tidal currents on wave propagation near an entrance to a harbor is a problem of interest in coastal engineering practice since it affects navigation safety, inlet entrance maintenance, jetty design, harbor performance, etc. Smith et al. (1998) conducted a laboratory study to investigate the wave–current interaction and the associated wave breaking in the presence of ebb currents in an idealized entrance. We use this case as an example to develop an understanding of the wave patterns that may be expected in such configurations. Since the hydraulic model measurements for waves, currents, and bathymetry were not detailed enough for a systematic model validation, a comparison can be performed only in a general sense. However, the comparison is sufficiently satisfactory and the numerical results are sufficiently informative (in fact, they shed more light on the phenomena than the laboratory data do) that they provide the motivation to supplement the hydraulic model study with numerical investigations of additional conditions of interest in this harbor engineering problem.

6.1. Summary of hydraulic model data

Fig. 11 (Smith et al., 1998) shows the overall arrangement of the physical model facility built at a prototype scale of 1:50. A wave maker is situated 24 m offshore at the head of

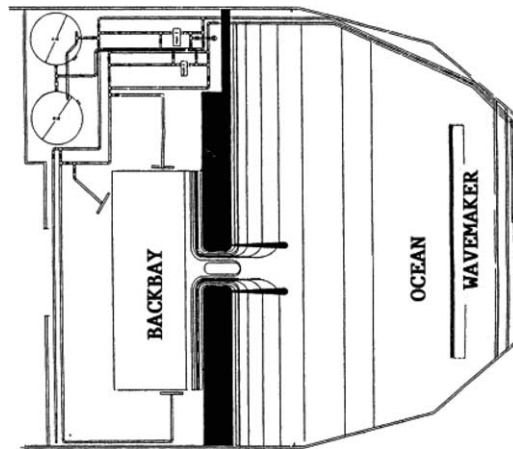


Fig. 11. Hydraulic model layout, idealized inlet facility (after Smith et al., 1998).

the model basin and currents can be generated by a pumping system. Fig. 12 shows the detailed geometry and bottom topography in the vicinity of the jettied inlet, where model simulations are focused. The idealized bathymetry is based on the design data for physical model construction. Most of the domain consists of a beach that slopes down to a depth of about 0.2 m, followed by a steep-slope leading to the deepwater end, where water depth is constant. Two parallel jetties are built to create an entrance channel, between which the depth is constant. This is preceded by a deep trench at the throat, which connects the backbay area (harbor) to the entrance channel. Experiments were limited to normally incident waves and ebb currents. Wave heights, currents, and water depths were measured at six gauges (Fig. 12) along the main channel. Laboratory runs were made using narrow-band unidirectional waves with desired target significant wave heights and peak periods. These are simulated numerically using a monochromatic representation with the associated significant wave heights and peak periods. This assumes that narrow-band unidirectional seas can be reasonably approximated by the equivalent monochromatic waves.

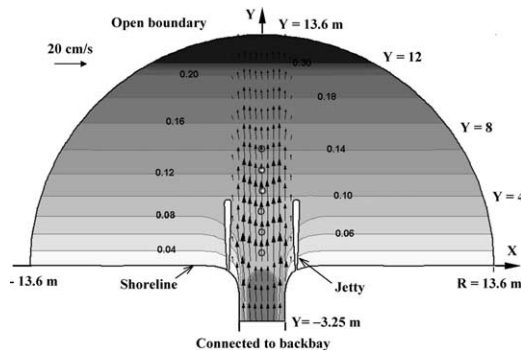


Fig. 12. Wave model domain, detailed bathymetry (depth in m), and underlying ebb current. Circles indicate gauge locations numbered from one at offshore to six near the inlet.

6.2. Flowfield simulation

A detailed current field was not available from hydraulic model study since measurements were made only at the locations shown in Fig. 12. A synthetic flow field had to be generated numerically to approximate the actual flow conditions in the laboratory. The two-dimensional circulation model DUCHESS, developed at TU Delft (Booij, 1989; Jin and Kranenburg 1993) was applied to a domain extending ± 30 m in the longshore direction and 30 m to the offshore direction, large enough to minimize any potential adverse lateral open boundary effects. The backbay area is not of interest for this study and was eliminated by placing a water boundary at the inlet throat ($y = -4$ m). The volume flux along this boundary with certain distribution was prescribed to drive the model for desired ebb-flow field. All offshore model boundaries are treated as flow-through (non-reflecting) using a radiation boundary condition. To prevent instabilities in the model solution, the volume flux was ramped up gradually from zero to a specified value, and was maintained constant, thereafter, until the current field in the entire modeling domain reached equilibrium. Input volume flux (which is unavailable from the hydraulic model data), bottom friction, and eddy viscosity were used as calibration coefficients in order to obtain the best fit between simulated currents and the data observed at the gauges.

The resulting jet-like ebb current field from model simulation is shown in Fig. 12. (For clarity, only a part of the flow model domain is shown). Detailed velocity profiles are provided in Fig. 13a along four transects across the mainstream of the ebb flow. The velocity distributions show a common structure of double-peak shear currents, with the shear structure intensifying from the offshore to a maximum near the middle of the throat, and then decreasing as a result of the specified flowfield being constant. Fig. 13b shows the variation of the current velocity along the centerline. A rapid change in velocity at near $y=0$ is due to the flow transition over a steep-slope from deep trench in the inlet throat to a shallow flat area between the jetties. Also in Fig. 13b, the simulated currents are compared to the measurements of two laboratory runs (Runs 3 and 4, described later) with the same target flow conditions, showing apparently good agreement in both cases. However, it is still uncertain how well the simulated current field represents the actual flow in the laboratory study. In particular, the limited data prevent us from confirming the lateral (shearing) structure of the ebb flow seen in Fig. 13a.

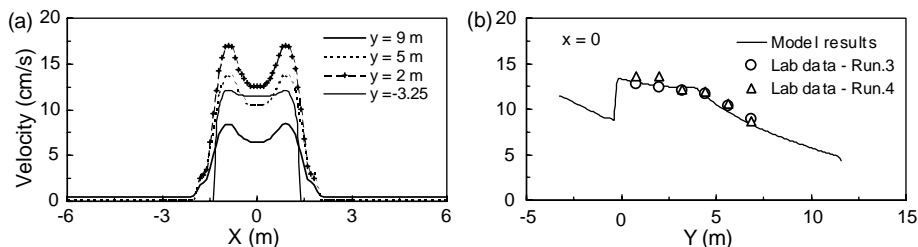


Fig. 13. Simulated current velocity profiles. (a) Longshore transects; (b) cross-shore transect, compared to lab data.

6.3. Simulation of normal wave incidence

We investigated two cases, without currents and with ebb currents, each of which consists of a large-wave case and a small-wave case. The target significant incident wave amplitude is 2.75 cm for large-waves and 1.83 cm for small-waves in the laboratory study. The wave period is 1.4 s for all cases. The computational domain for wave simulations, shown in Fig. 12, consists of 165,371 triangular elements and 83,581 nodes (representing a resolution of 20 nodes per wavelength), and the radius of the semicircular boundary is 13.6 m. All shoreline and jetty boundaries are considered non-reflecting and assigned the new boundary condition (15) for absorbing outgoing waves. The advantage of the direction-dependent boundary condition described in Section 2 can be demonstrated in this application, since the incident wave angles along much of the jetty boundaries are likely to be large. This is demonstrated in Fig. 14 for the case of normal wave incidence and no ambient current. Fig. 14b shows that spurious reflections seen in Fig. 14a beyond the tips of the jetties have disappeared, and waves can follow the sidewalls of the jetties smoothly as they propagate into the inlet. Fig. 15 compares these results with hydraulic model measurements and indicates that model estimates with the new boundary condition have a somewhat better match to the data. Obviously, with the boundary condition (15) that accommodates outgoing wave directionality in a nonlinear manner, the model estimates are much improved.

Model results for the cases of no currents are presented and compared to the data in Fig. 16. Runs 1 and 2 correspond, respectively, to large- and small-wave incidence. Because of the uncertainties in the hydraulic model associated with establishing the targeted (as opposed to the actual) incident wave heights, different incident values were tried until the best match was achieved at the offshore-most gauge (Gauge 1). Fig. 16 shows that model predictions overestimate the data when the target significant wave heights are used as the incident wave conditions. With smaller amplitudes $A_i = 2.5$ and 1.65 cm for Runs 1 and 2, the best results are obtained relative to the data at all gauges except for Gauge 2. Note that data at Gauge 2 are consistently lower than model estimates for all conditions (Fig. 18, see Section 6.4 for further discussion).

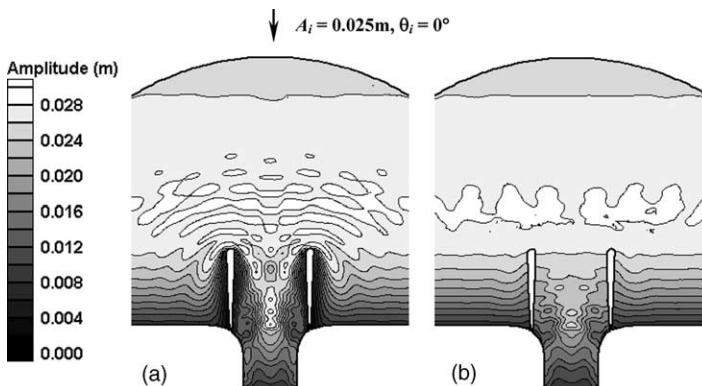


Fig. 14. Simulated wave amplitudes, jettied inlet without current. (a) Conventional boundary condition; (b) improved boundary condition.

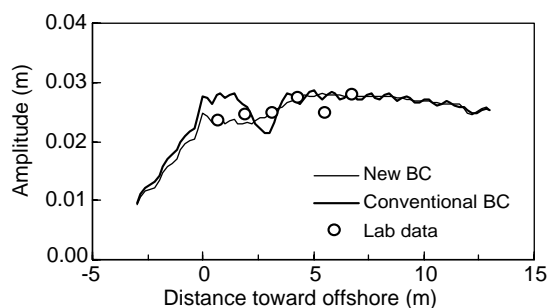


Fig. 15. Model results of wave amplitudes at central transect, compared to lab data.

For ebb currents, model estimates were made using adjusted wave amplitudes of 2.5 cm (Run 3) and 1.65 cm (Run 4). Based on the results for Run 3 (Fig. 17), the model captures the bending effect inflicted on the crests by the opposing currents (Fig. 17a); the phase pattern in the middle of the entrance channel indicates wave crossing and focusing (as in the case of shoals, Berkhoff et al., 1982). Waves heights are amplified not only by the opposing currents, but also by the increasing focusing due to current shear, which creates a high-wave zone in the middle of the domain (Fig. 17b). The width of the high-wave zone decreases along the centerline towards the middle of the entrance channel, where waves cross, leaving large shadow areas near the jetty walls. Fig. 18 shows that, for both large- and small-wave incidence (Runs 3 and 4), following the centerline, waves increase rapidly in amplitude and become large enough to break. The first wave breaking occurs further offshore ($y \cong 6.5$ m) for the large-wave case, compared to $y \cong 4.5$ m for both the small-wave case and the no current case (Fig. 16a). Continued strong focusing by the underlying currents in the deep, flat, and narrow channel between the jetties results in renewed growth until a second wave breaking occurs at $y \cong 2.4$ m.

Model results for Runs 3 and 4 provide fair agreement with the laboratory data (Fig. 18), although they are not as good as that without currents; the predicted wave amplitudes are generally higher than the data. As noted above, the uncertainty of the actual current field used in the model compared to the laboratory condition is perhaps the main reason for the discrepancies. Also, we were unable to explain why Gauge 2 measurements for all test conditions were consistently lower than model estimates. If instrumentation

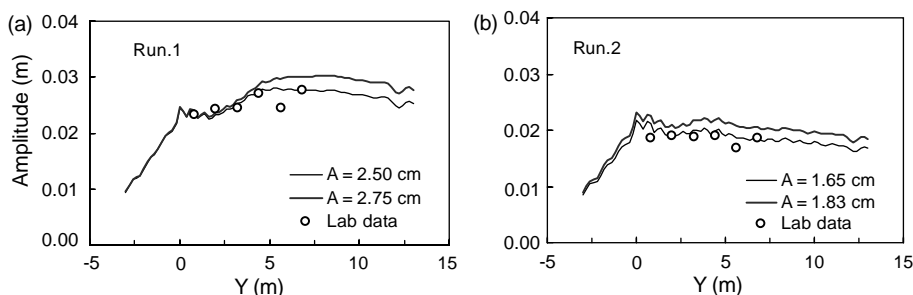


Fig. 16. Wave amplitudes along the centerline, jettied inlet case, normally incident waves without current.

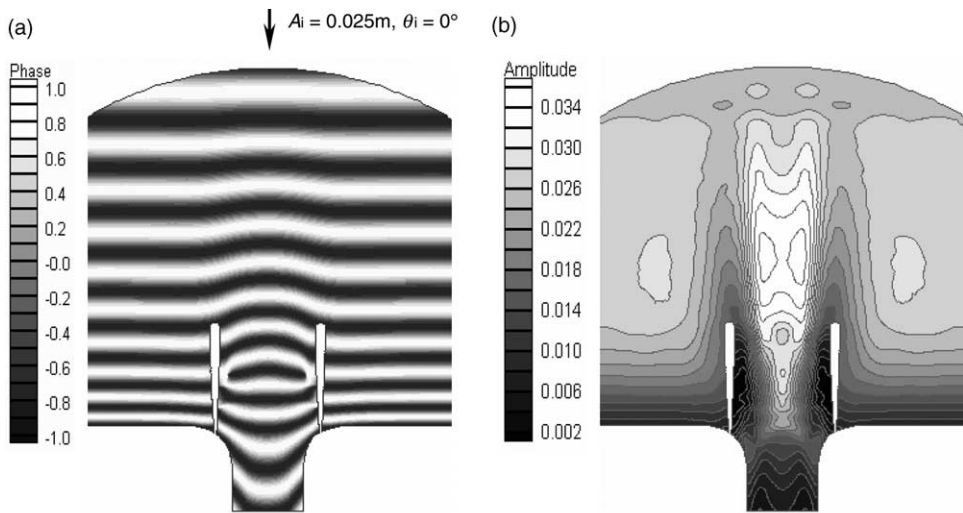


Fig. 17. Model results for a jettied inlet case, with ebb current. (a) Phase; (b) amplitude.

errors were involved at this gauge, we would have lost important information about the onset of wave breaking. Yet, as Fig. 17 reveals, an intricate wave pattern may be expected near harbor entrances with jetties; it also suggests, however, that many more measurements would be needed to identify any meaningful features of the wave–current interaction in the hydraulic model.

6.4. Oblique wave incidence

Since there are no data available for oblique wave incidence from the hydraulic model study, we investigate the effect of ebb and flood currents on wave transformation. Fig. 19 shows numerical results for two simulations, i.e. for 45° incidence ($A_i = 2.5$ cm)

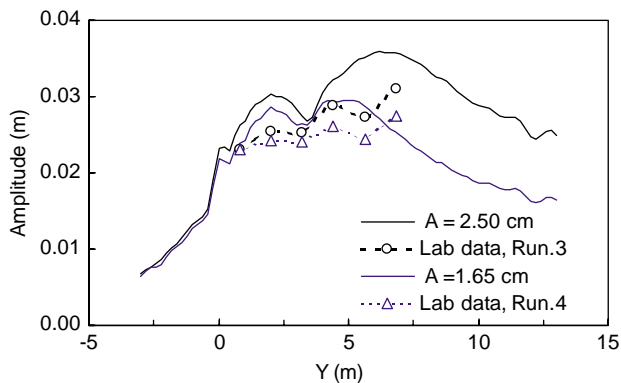


Fig. 18. Wave amplitudes along the centerline, jettied inlet case; normal waves with ebb currents.

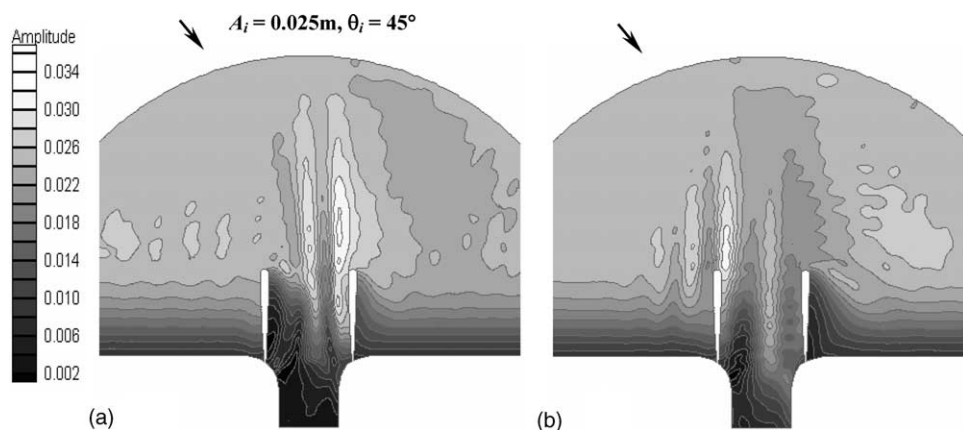


Fig. 19. Simulated amplitudes for oblique wave incidences, jettied inlet case. (a) With ebb current; (b) with flood current.

encountering an ebb current and a flood current. The representing flood current is assumed to be simply the reverse of the ebb current for the purposes of this case study.

Oblique waves are refracted to varying degrees when they come across the ebb flow that, as shown in Figs. 12 and 13, has a structure with changing shear intensity. As shown in Fig. 19a, the double-peak shear current causes wave focusing and diverging, which generates two elongated low-wave and two high-wave zones in the central area. Fig. 20b clearly indicates this large fluctuation in the wave amplitudes across the ebb stream, with two peaks corresponding to wave focusing due to increasing current shear. Compared to the case of normal wave incidence (Fig. 20a), peak waves in the flow zone are much weaker (also see Fig. 21).

With flood currents, the strong current shear near the left edge of the flood stream does not allow oblique waves to fully penetrate into the flow zone (McKee, 1974). Consequently, part of the wave energy is reflected toward the left (Fig. 19b), causing large fluctuations of wave amplitude on the left side of the mainstream (Fig. 20b). The fact that similar effects were obtained in the vortex ring test lends credence to these results. The transmitted part of waves is subject to refraction by the flood current, and, as in the case with ebb currents, results in large variation in wave amplitudes inside the flow zone. For flood currents, the wave amplitudes are much lower in the flow zone outside the tip of

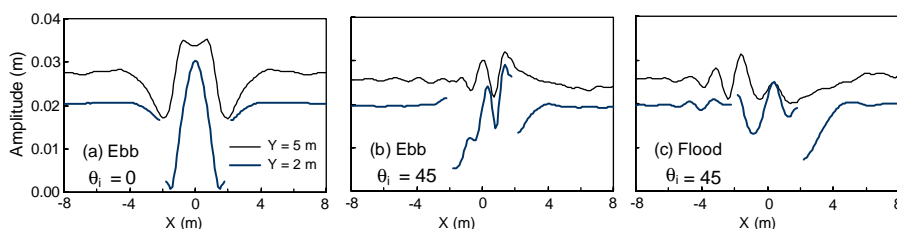


Fig. 20. Simulated wave amplitudes along two lateral transects, jettied inlet case ($A_i = 0.025$ m).

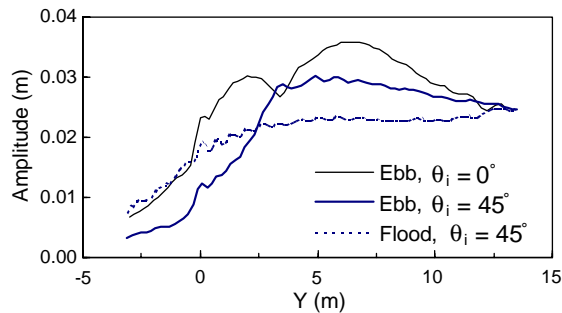


Fig. 21. Simulated wave amplitudes along the centerline, jettied inlet case ($A_i=0.025$ m).

jetties because of wave reflection at the left edge of the mainstream (Figs. 19b and 21) and also because the waves are following the currents. In spite of this, more wave energy is able to penetrate into the jetty channel and the inlet compared to the ebb current case, either with normal or oblique incidence (Fig. 21). This is because flood currents have turned the waves more toward the inlet, and that lower wave amplitudes have resulted in less wave energy dissipation (breaking) in the channel and inlet area between jetties.

7. Concluding remarks

We have provided a comprehensive treatment of the various issues associated with finite-element modeling of the elliptic wave–current interaction equation. Methods to effectively handle various nonlinear aspects of the solution are developed. Implementation of an improved boundary absorption condition that accounts for the angle of wave approach and the local bathymetric variation has largely eliminated the spurious oscillations commonly seen in the solutions of similar models. The model developed on the basis of the methods detailed here was applied to three wave–current interaction cases. The results were found to be consistent with those of other published models.

Relative to the frequently used parabolic approximation models (e.g. Yoon and Liu, 1989), the present results are nearly identical in some cases. In other cases, the limitations of the parabolic approximations are illustrated, such as the effect of dropping the second-order derivative when the wave height changes rapidly (as in the rip-current test-case). Also, the reflective pattern seen in the elliptic model results as a consequence of a highly oblique angle at which waves approach the current field permits one to speculate that parabolic approximations may be inadequate in the case of strong velocity shears, where large-angle wave refraction, diffraction, and even reflection (due to wave caustics) may be expected. Relative to Boussinesq models, which have traditionally been applicable only to shallow water waves¹ the present approach suffers, in principle, from the disadvantage of inadequate representation of nonlinear shallow-water effects. However, the results obtained here show only minor discrepancies, and even those are somewhat diminished

¹ The applicability of Boussinesq models is now being extended to intermediate and deep water depths.

through the use of the nonlinear dispersion relation (5). Also, a strategy for including wave–wave interactions in elliptic finite element models and some preliminary results have been described in Panchang and Demirbilek (2001). Since multiple nonlinear mechanisms have been successfully handled in the work reported here, incorporating the additional mechanism of wave–wave interaction may not be problematic. Further, a finite-element formulation that can better represent complex geometries (such as the case of jettied inlets) is more conducive to the time-independent elliptic formulation (8) than to the time-dependent and highly nonlinear Boussinesq models.

The satisfactory solutions obtained for the tests described in Section 5 prompted the investigation of wave–current interactions near a jettied tidal inlet, a problem of considerable engineering importance (e.g. Lin and Demirbilek, *in press*; Smith et al., 1998). The wave patterns are seen to be quite intricate. Ebb currents lead to considerable breaking outside the entrance channel, but renewed wave growth occurs due to focusing by the currents before the waves break again. For flood tides, the wave heights are smaller outside the jetty channel, as a consequence of the non-opposing nature of the waves and currents, but they are larger than in the ebb current case inside the channel because waves do not break. Although the case investigated here dealt with the layout constructed by Smith et al. (1998), the overall results presented here have set the stage for tackling practical engineering problems.

The solution methods proposed here require only moderate computer power. The examples illustrated show that a typical application involving monochromatic wave transformation would take about 15 min of run time on a modern PC.

Acknowledgements

Partial support for this work was received from the Office of Naval Research, the Army Corps of Engineers, the Maine Sea Grant Program, and the National Sea Grant Office. We are grateful to Professor Q. Chen of the University of South Alabama for providing the flow field for one of the rip current cases investigated. Assistance provided by Messrs K. Schlenker, K. Zubier, and L. Zhao is acknowledged.

References

- Arthur, R.S., 1950. Refraction of shallow water waves: the combined effect of currents and under water topography. *EOS Trans.* 31, 549–552.
- Battjes, J.A., Janssen, J., 1978. Energy loss and set-up due to breaking of random waves, *Proceedings of the 16th International Conference Coastal Engineering*. ASCE, New York, pp. 569–587.
- Beltrami, G.M., Bellotti, G., De Girolamo, P., Sammarco, P., 2001. Treatment of wave breaking and total absorption in a mild-slope equation FEM model. *J. Waterw., Port, Coastal Ocean Eng.* 127, 263–271.
- Berkhoff, J.C.W., 1972. Computation of combined refraction and diffraction, *Proceedings of the 13th International Conference Coastal Engineering*. ASCE, New York.
- Berkhoff, J.C.W., Booy, N., Radder, A.C., 1982. Verification of numerical wave propagation models for simple harmonic linear water waves. *Coastal Eng.* 6, 255–279.

- Booij, N., 1981. Gravity waves on water with non-uniform depth and current. Technical Report 81-1, Department of Civil Enging, Delft University of Technology, The Netherlands.
- Booij, N., 1989. User manual for the program DUCHESS. Technical Report, Delft University of Technology, The Netherlands.
- Booij, N., Ris, R.C., Holthuijsen, L.H., 1999. A third-generation wave model for coastal regions. 1. Model description and validation. *J. Geophys. Res.* 104 (c4), 7649–7666.
- Chamberlain, P.G., Porter, D., 1995. The modified mild-slope equation. *J. Fluid Mech.* 291, 393–407.
- Chen, W., 2002. Finite element modeling of wave transformation in harbors and coastal regions with complex bathymetry and ambient currents. PhD dissertation, Department of Civil Engineering, University of Maine, Orono. USA.
- Chen, Q., Dalrymple, R.A., Kirby, J.T., Kennedy, A.B., Haller, M.C., 1999. Boussinesq modeling of a rip current system. *J. Geophys. Res.* 104 (c9), 20617–20637.
- Chen, W., Panchang, V.G., Demirebilek, Z., 2002. A generalized absorbing boundary condition for elliptic harbor wave models, Proceedings of the 4th International Symposium on Ocean Wave Measurement and Analysis, vol. 1. ASCE, New York, pp. 714–723.
- Dally, W.R., Dean, R.G., Dalrymple, R.A., 1985. Wave height variation across beaches of arbitrary profile. *J. Geophys. Res.* 90 (c6), 11917–11927.
- De Girolamo, P., Kostense, J.K., Dingemans, M.W., 1988. Inclusion of wave breaking in a mild-slope model. In: Schrefler, Zienkiewicz (Eds.), *Computer Modeling in Ocean Engineering*. Balkema, Rotterdam, pp. 221–229.
- Grassa, J.M., Flores, J., 2001. Discussion of: 'Maa, J.P.-Y.; Hsu, T.-W.; Tsai, C.H., Juang, W.J., 2000. Comparison of Wave Refraction and Diffraction Models'. *J. Coastal Res.* 17 (3), 762.
- Isaacson, M., Qu, S., 1990. Waves in a harbour with partially reflecting boundaries. *Coastal Eng.* 14, 193–214.
- Kirby, J.T., 1984. A note on linear surface wave–current interaction over slowly varying topography. *J. Geophys. Res.* 89 (c1), 745–747.
- Kirby, J.T., 1989. A note on parabolic radiation boundary conditions for elliptic wave calculation. *Coastal Eng.* 13, 211–218.
- Kirby, J.T., Dalrymple, R.A., 1986. An approximate model for nonlinear dispersion in monochromatic wave propagation models. *Coastal Eng.*, 9, 545–561.
- Kirby, J.T., Dalrymple, R.A., 1994. Combined refraction/diffraction model REF/DEF 1, version 2.5, documentation and user's manual. Research Report No. CACR-94-22, Department of Civil Engineering, University of Delaware.
- Kostense, J.K., Dingemans, M.W., van den Bosch, P., 1988. Wave–current interaction in harbours, Proceedings of the 21th International Conference Coastal Engineering, vol. 1. ASCE, New York pp. 32–46.
- Li, B., 1994. A generalized conjugate gradient model for the mild slope equation. *Coastal Eng.* 23, 215–225.
- Li, B., Anastasiou, K., 1992. Efficient elliptic solvers for the mild-slope equation using the multigrid method. *Coastal Eng.* 16, 245–266.
- Lin, L., Demirebilek, Z., 2005. Evaluation of two numerical wave models by inlet physical model. To appear *J. Waterw., Port, Coastal Ocean Eng* 131(3), in press.
- Liu, P.L.-F., 1983. Wave–current interactions on a slowly varying topography. *J. Geophys. Res.* 88 (c7), 4421–4426.
- Liu, P.L.-F., 1990. Wave transformation. In: Le Mehaute, B., Hanes, D.M. (Eds.), *The Sea Ocean Engineering Science*, vol. 9. Wiley, New York, p. 1301 (B. LeMehaute, D. Hanes, eds.).
- Liu, T.K., Peng, C.Y., Schumacher, J.D., 1994. Wave–current interaction study in the Gulf of Alaska for detection of eddies by sythetic aperture radar. *J. Geophys. Res.* 99 (c5), 10075–10085.
- Madsen, P.A., Sørensen, O.R., 1992. A new form of the Boussinesq equations with improved linear dispersion characteristics. Part 2: a slowly-varying bathymetry. *Coastal Eng.* 18, 183–205.
- Mapp, G.R., Welch, C.S., Munday, J.C., 1985. Wave reflection by warm core rings. *J. Geophys. Res.* 90, 7153–7162.
- McKee, W.D., 1974. Waves on a shearing current: a uniformly valid asymptotic solution. *Proceedings of the Cambridge Philosophical Society* 75, 295–301.
- Nwogu, O., 1993. Alternative form of Boussinesq equations for nearshore wave propagation. *J. Waterw., Port, Coastal Ocean Eng.* 119, 618–638.

- Oliveira, F.S.B.F., Anastasiou, K., 1998. An efficient computational model for water wave propagation in coastal regions. *Appl. Ocean Res.* 20, 263–271.
- Panchang, V.G., Demirebilek, Z., 2001. Simulation of waves in harbors using two-dimensional elliptic equation models. In: Liu, P. L.-F. (Ed.), *Advances in Coastal and Ocean Engineering*, vol. 7. World Scientific, pp. 125–162.
- Panchang, V.G., Ge, W., Cushman-Roisin, B., Pearce, B.R., 1991. Solution to the mild-slope wave problem by iteration. *Appl. Ocean Res.* 13 (4), 187–199.
- Panchang, V.G., Xu, B., Demirebilek, Z., 1998. Wave prediction models for coastal engineering applications. In: Herbich, J.B. (Ed.), *Developments in Offshore Engineering*. Gulf Publishing Co., Book Div., Houston, pp. 163–194 chapter 4.
- Panchang, V.G., Chen, W., Xu, B., Schlenker, K., Demirebilek, Z., Okihiro, M., 2000. Effects of exterior bathymetry in elliptic harbor wave models. *J. Waterw., Port, Coastal Ocean Eng.* 126 (2), 71–78.
- Peregrine, D.H., Smith, R., 1975. Stationary gravity waves on non-uniform free streams: jet-like flows. *Math. Proc. Cambridge Phil. Soc.* 77, 415–438.
- Radder, A.C., 1992. Efficient Elliptic Solvers for the Mild-slope equation using the multigrid method, by B. Li, K. Anastasiou: comments. *Coastal Eng.* 18, 347–352.
- Resio, D.T., 1993. STWAVE: wave propagation simulation theory, testing and application. Department of Oceanography, Ocean Engineering, and Environmental Science, Florida Institute of Tech..
- Ris, R.C., Holthuijsen, L.H., Booij, N., 1999. A third-generation wave model for coastal regions. 2. verification. *J. Geophys. Res.* 104 (c4), 7667–7681.
- Smith, J.M., Seabergh, W.C., Harkins, G.S., Briggs, M.J., 1998. Wave breaking on a current at an idealized inlet. Rept. CHL-98-31, US Army Corps of Engineers, Vicksburg, MS 39180.
- Steward, D.R., Panchang, V.G., 2001. Improved coastal boundary conditions for water wave simulation models. *Ocean Eng.* 28, 139–157.
- Van der Vorst, H.A., 1992. Bi-CGSTAB: a fast and smoothly converging variant of Bi-CG for the solution of nonsymmetric linear systems. *SIAM J. Sci. Stat. Comput.* 13, 631–644.
- Vogel, J.A., Radder, A.C., de Reus, J.H., 1988. Verification of numerical wave propagation models in tidal inlet, *Proceedings of the 23th International Conference Coastal Engineering*. ASCE, Malaga, Spain.
- Wei, G., Kirby, J.T., Grilli, S.T., Subramanya, R., 1995. A fully nonlinear Boussinesq model for surface waves, 1. Highly nonlinear unsteady waves. *J. Fluid Mech.* 294, 71–92.
- Xu, B., Panchang, V.G., Demirebilek, Z., 1996. Exterior reflections in elliptic harbor wave models. *J. Waterw., Port, Coastal Ocean Eng.* 122 (3), 118–126.
- Yoon, S., Liu, P.L.-F., 1989. Interactions of currents and weakly nonlinear water waves in shallow water. *J. Fluid Mech.* 205, 397–419.
- Zhao, L., Panchang, V.G., Chen, W., Demirebilek, Z., Chhabbra, N., 2001. Simulation of breaking effects in a two-dimensional harbor wave prediction model. *Coastal Eng.* 42, 359–373.
- Zubier, K., Panchang, V.G., Demirebilek, Z., 2003. Simulation of waves at Duck (North Carolina) using two numerical models. *Coastal Eng. J.* v45 (3), 439–469.
- Zundel, A.K., Fugal, A.L., Jones, N.L., Demirebilek, Z., 1998. Automatic definition of two-dimensional coastal finite element domains. In: Babovic, V., Larsen, L.C. (Eds.), *Proceedings of the 3rd International Conference Hydroinformatics*. A.A. Balkema, Rotterdam, pp. 693–700.